J|A|C|S
ARTICLES
Published on Web 01/30/2007

Crystal Chemistry and Electronic Structure of the Metallic Lithium Ion Conductor, LiNiN

Zlatka Stoeva,[†] Bernd Jäger,[‡] Ruben Gomez,[†] Sabri Messaoudi,[§] Mouna Ben Yahia,[§] Xavier Rocquefelte,[§] Gary B. Hix,[||] Walter Wolf,[⊥] Jeremy J. Titman,[†] Régis Gautier,[§] Peter Herzig,[‡] and Duncan H. Gregory*[,#]

Contribution from the School of Chemistry, University of Nottingham, University Park, Nottingham NG7 2RD, U.K., Institut für Physikalische Chemie, Universität Wien, Währinger Strasse 42, 1090 Vienna, Austria, Sciences Chimiques de Rennes, UMR 6226, CNRS - ENSC Rennes, Campus de Beaulieu, 35700 Rennes, France, School of Biomedical and Natural Science, Nottingham Trent University, Clifton Lane, Nottingham NG11 8NS, U.K., Materials Design s.a.r.l., 44 Avenue F-A. Bartholdi, 72000 Le Mans, France, and WestCHEM, Department of Chemistry, Joseph Black Building, University of Glasgow, Glasgow G12 8QQ, U.K.

Received May 8, 2006; E-mail: d.gregory@chem.gla.ac.uk

Abstract: The layered ternary nitride LiNiN shows an interesting combination of fast Li^+ ion diffusion and metallic behavior, properties which suggest potential applications as an electrode material in lithium ion batteries. A detailed investigation of the structure and properties of LiNiN using powder neutron diffraction, ab initio calculations, SQUID magnetometry, and solid-state NMR is described. Variable-temperature neutron diffraction demonstrates that LiNiN forms a variant of the parent Li_3N structure in which Li^+ ion vacancies are ordered within the [LiN] planes and with Ni exclusively occupying interlayer positions (at 280 K: hexagonal space group $P\bar{6}m2$, $a = 3.74304(5)$ Å, $c = 3.52542(6)$ Å, $Z = 1$). Calculations suggest that LiNiN is a one-dimensional metal, as a result of the mixed π- and σ-bonding interactions between Ni and N along the *c*-axis. Solid-state ^{7}Li NMR spectra are consistent with both fast Li^+ motion and metallic behavior.

Introduction

Lithium nitridometallates have attracted significant interest recently because of their unusual structures and electronic properties, complemented by their promising electrochemical performance. The potential of lithium nitridometallates as anode materials in rechargeable lithium batteries has been demonstrated, and capacity values in the range 700−800 mA h g^{-1} are reported.[1,2] Therefore, a more detailed understanding of the fundamental properties of these materials is desirable, particularly with a view to improving their electrochemical characteristics.

The layered nitridometallate LiNiN[3] is particularly interesting because it contains a high number of inherent Li^+ vacancies, as well as infinite, straight $^1_\infty[NiN_{2/2}]^-$ chains which are expected to promote one-dimensional (1D) electronic properties. We reported a preliminary study of Li^+ ion diffusion in this material recently.[4] Structurally, LiNiN[3] is related to the disordered phases $Li_{3-x-y}M_xN$ (M = Cu, Ni, Co; y = Li^+ vacancy) in which the transition metal atoms substitute at the interplanar Li(1) site in the parent Li_3N structure.[5] The high substitution level ($x = 1$) in LiNiN suggests that Ni completely replaces Li on the Li(1) site,[3,4] and this has important implications for the electronic and ion-transport properties. The variation with temperature of the wide-line ^{7}Li NMR spectrum of LiNiN differs significantly from that observed for the parent Li_3N, suggesting that Li^+ ion diffusion is quite different in these two materials despite the similarity in their structures. It should be noted, however, that for the disordered $Li_{3-x-y}Cu_xN$ phases even the highest values of x result in wide-line ^{7}Li NMR spectra which are almost identical to those for Li_3N.[6]

LiNiN can be compared with other ternary nitrides which contain straight 1D Ni−N chains, leading to low coordination numbers and low-spin states for Ni, as well as interesting electronic and magnetic properties. CaNiN[7] and $Li_3Sr_3Ni_4N_4$,[8] for example, contain $^1_\infty[NiN_{2/2}]^{2-}$ chains with formal Ni^{1+} ions in a d^9 configuration, such that the chain is one electron short of filling the d−p bands. This configuration might be expected to promote anti-ferromagnetic interactions along the chains and to exhibit spin Peierls instability, leading to superstructure

[†] University of Nottingham.
[‡] Universität Wien.
[§] CNRS - ENSC Rennes.
[||] Nottingham Trent University.
[⊥] Materials Design s.a.r.l.
[#] University of Glasgow.

(1) Nishijima, M.; Kagohashi, T.; Imanishi, M.; Takeda, Y.; Yamamoto, O.; Kondo, S. *Solid State Ionics* **1996**, *83*, 107.
(2) Shodai, T.; Okada, S.; Tobishima, S.; Yamaki, J. *Solid State Ionics* **1996**, *86−88*, 785.
(3) Barker, M. G.; Blake, A. J.; Edwards, P. P.; Gregory, D. H.; Hamor, T. A.; Siddons, D. J.; Smith, S. E. *Chem. Commun.* **1999**, 1187.
(4) Stoeva, Z.; Gomez, R.; Gordon, A. G.; Allan, M.; Gregory, D. H.; Hix, G. B.; Titman, J. J. *J. Am. Chem. Soc.* **2004**, *126*, 4066.
(5) (a) Sachsze, W.; Juza, R. Z. *Anorg. Allg. Chem.* **1949**, *259*, 278. (b) Niewa, R.; Huang, Z.-L.; Schnelle, W.; Hu, Z.; Kniep, R. Z. *Anorg. Allg. Chem.* **2003**, *629*, 1778.
(6) Stoeva, Z.; Gomez, R.; Gregory, D. H.; Hix, G. B.; Titman, J. *J. Dalton Trans.* **2004**, *19*, 3093.
(7) Chern M. Y.; DiSalvo, F. J. *J. Solid State Chem.* **1990**, *88*, 459.
(8) Gudat, A.; Kniep, R.; Rabenau, A. Z. *Anorg. Allg. Chem.* **1991**, *597*, 61.

10.1021/ja063208e CCC: $37.00

formation. Of the nitrides containing $^1_\infty[NiN_{2/2}]^{2-}$ chains, CaNiN is the most studied. Perhaps unexpectedly, CaNiN is metallic, and no anomalies in the resistivity and magnetic susceptibility have been observed.[7] The electronic structure of CaNiN has been studied a number of times since the discovery of the nitridonickelate.[9−12] The initial DFT calculations attributed the absence of distortions to 2D and 3D interchain coupling and a low likelihood of Fermi surface-driven charge density wave (CDW) or spin density wave (SDW) instabilities.[9] Subsequent studies acknowledge the more than peripheral significance of Ca interactions with the $^1_\infty[NiN_{2/2}]^{2-}$ chains in suppressing such instabilities.[11,12] There are perhaps two important distinctions between CaNiN and LiNiN which may influence the electronic structure and behavior of the lithium compound. First, formal electron counting suggests the formulation LiNi(II)N, although the charge balance may be achieved by the formation of holes in bands dominated by N states as proposed for $Li_{3-x}Co_xN$ compounds.[13] Second, by contrast to CaNiN, all the $^1_\infty[NiN_{2/2}]^{n-}$ chains in LiNiN are parallel, and none are spatially separated by a layer of electropositive atoms (ions).

The preliminary evidence for fascinating electronic properties combined with fast Li^+ ion diffusion prompted us to carry out a more detailed investigation. Powder neutron diffraction (PND) has allowed us to make more definitive conclusions about the structure of LiNiN, particularly in terms of nickel substitution levels and the distribution of Li^+ vacancies. The structural study clarifies the subtle differences between LiNiN and the disordered $Li_{3-x-y}Ni_xN$ phases and presents us with the starting point for our density functional theory (DFT) calculations of the band structure. These calculations combined with new results from magic angle spinning ^{7}Li NMR support the postulated 1D metallic behavior of LiNiN.

Experimental Section

Synthesis. The binary compound Li_3N was synthesized by reaction of molten Li−Na alloy with dried nitrogen at 450 °C for 3−4 days.[3] Na is used as an inert solvent in the reaction and was subsequently removed by vacuum distillation at 400−450 °C for 24 h. The product, a highly crystalline red-purple powder, was identified as Li_3N using powder X-ray diffraction (ICDD PDF database Card No. 30-759). LiNiN was prepared by reaction of Li_3N with nickel foil which was reduced before use in 20% H_2/N_2 gas for 24 h at 600 °C. For this reaction, Li_3N powder is placed in the Ni foil tube, which is then sealed in a reaction vessel under nitrogen at ambient pressure and heated at 730−750 °C for 7 days.[3,4] Under these conditions, Li_3N reacts with the surface of the nickel foil, forming a green-black/gold layer of highly crystalline powder with metallic luster. This layer can be easily removed from the surface of the foil and subsequently characterized. All starting materials and products were handled in a nitrogen-filled recirculating glovebox (Saffron Scientific; $O_2 < 1$ ppm, $H_2O < 5$ ppm).

Powder X-ray Diffraction. Initially, the products of the reaction were examined by powder X-ray diffraction (PXD) using a Philips XPERT ($\theta-2\theta$) diffractometer with Cu Kα radiation. The air- and moisture-sensitive samples were sealed in custom-designed sample holders during data collection. Phase purity was examined from 2-h scans over the range 5°−100° 2θ in Bragg−Brentano geometry. The experimental patterns were compared to a calculated pattern derived from single-crystal structural data using the PowderCell 2.3 package.[14] The reaction as described above leads to high-purity bulk samples of LiNiN. Rietveld refinements of the PXD data were carried out using the General Structure Analysis System (GSAS)[15] for data collected over 12-h scans at ambient temperature. Refinements using the single-crystal structural model gave good profile fits. However, given the weak X-ray scattering of Li, different models for Li^+ vacancy distribution could not be tested accurately. Additionally, the PXD data suffered from strong preferred orientation effects which were evident from the changes of the relative intensities for different scans of the same sample. Therefore, the refinements of the PXD data are not discussed further here. PXD was, however, routinely used to verify the purity of the samples before and after other measurements.

Powder Neutron Diffraction. Time-of-flight (TOF) PND data were collected using the high-intensity diffractometer POLARIS at the ISIS spallation source in the Rutherford Appleton Laboratory. Variable-temperature data were collected to coincide with the temperature range of the ^{7}Li solid-state NMR measurements (see below). The powder sample (~1 g) was contained in a 6 mm diameter, thin-walled, cylindrical vanadium sample can. The can was loaded in a nitrogen-filled glove box and sealed with an indium gasket prior to transfer to a helium cryostat (AS Scientific Instruments, Abingdon). Neutron diffraction data were collected at 100, 200, and 280 K using the three fixed detector banks consisting of either ^{3}He gas tubes at $\langle 2\theta\rangle = 35°$ and $\langle 2\theta\rangle = 145°$, and ZnS scintillator at $\langle 2\theta\rangle = 90°$. The temperatures of the samples were monitored using a RhFe sensor attached to the outside wall of the vanadium sample cans. Rietveld refinement against PND data was performed using GSAS.[15] Data from all three detector banks were used simultaneously in the final least-squares cycles for each refinement. Peak shapes were modeled using the type-3 profile function in GSAS which is a convolution of back-to-back exponentials with a pseudo-Voigt function. The background was modeled using an exponential expansion function (background function 6 in GSAS) which accounts for contributions at both low and high Q. PND data refinements were started by fitting the background coefficients, scale factor, lattice parameters, and peak shapes and subsequently introduced atomic parameters and absorption factors. After the refinements had stabilized, thermal coefficients were varied anisotropically. No impurity phases were detected in the PND data. The vanadium sample can and the vacuum windows in the cryostat yielded a group of reflections that were excluded from the refinements. These excluded regions did not contain reflections arising from the compound under study.

Ab Initio Calculations. Initial ab initio DFT[16,17]calculations of the LiNiN band structure used the full-potential linearized augmented-plane-wave (FLAPW) method,[18−20] adopting an exchange and correlation potential by Hedin and Lundqvist.[21,22] The lattice parameters were set to the values obtained from PND at 280 K (see below), and the muffin-tin radii were fixed to values of 0.7978 Å, 0.8780 Å, and 0.8848 Å for Li, Ni, and N, respectively. For the l expansion for the potential and the electron densities within the muffin-tin spheres terms up to $l = 8$ were considered. Plane waves for the construction of the wave functions in the interstitial were included up to a length for the corresponding **k**

(9) Massidda, S.; Pickett, W. E.; Posternak, M. *Phys. Rev. B: Condens. Matter Mater. Phys.* **1991**, *44*, 1258.
(10) Mattheis, L. F. *Phys. Rev. B: Condens. Matter Mater. Phys.* **1993**, *47*, 8224.
(11) Green, M. T.; Hughbanks, T. *Inorg. Chem.* **1993**, *32*, 5611.
(12) Springborg, M.; Albers, R. C. *Phys. Rev. B: Condens. Matter Mater. Phys.* **2004**, *69*, 235115.
(13) (a) Suzuki, S.; Shodai, T.; Yamaki, J. *J. Phys. Chem. Solids* **1998**, *59*, 331. (b) Shodai, T.; Sakurai, Y.; Suzuki, T. *Solid State Ionics* **1999**, *122*, 85.
(14) Nolze, G.; Kraus, W. *Powder Diffr.* **1998**, *13*, 256.
(15) Larson, A. C.; von Dreele, R. B. The General Structure Analysis System, Los Alamos National Laboratories, Report LAUR 086-748; LANL: Los Alamos, NM, 2000.
(16) Hohenberg, P.; Kohn, W. *Phys. Rev.* **1964**, *136*, 864.
(17) Kohn, W.; Sham, L. J. *Phys. Rev.* **1965**, *140*, 1133.
(18) Koelling, D. D.; Arbman, G. O. *J. Phys. F: Met. Phys.* **1975**, *5*, 2041.
(19) Wimmer, E.; Krakauer, H.; Weinert, M.; Freeman, A. J. *Phys. Rev. B: Condens. Matter Mater. Phys.* **1981**, *24*, 864.
(20) Jansen, H. J. F.; Freeman, A. J. *Phys. Rev. B: Condens. Matter Mater. Phys.* **1984**, *30*, 561.
(21) Hedin, L.; Lundqvist, B. I. *J. Phys. C: Solid State Phys.* **1971**, *4*, 2064.
(22) Hedin, L.; Lundqvist, S. *J. Phys. (Paris)* **1972**, *33*, C3−C73.

vector of 4.0 (in units of $2\pi/a$), corresponding to ~320 basis functions per unit cell or per formula unit. For the self-consistency procedure a $19 \times 19 \times 19$ Monkhorst and Pack mesh[23] was used for the valence states, while the higher-lying Ni core states (3s and 3p) as well as the Li 1s states were treated as band states in a second energy window using a $9 \times 9 \times 9$ Monkhorst and Pack mesh (corresponding to 400 and 60 k points, respectively). The electric-field gradients (EFGs) were calculated from the $l = 2$ component of the Coulombic potential very close to the nuclear sites using the formalism by Herzig[24] and Blaha et. al.[25]

The Fermi surface was calculated within the MedeA computational platform[26] making use of the integrated Vienna ab initio simulation package (VASP).[27−29] The generalized gradient approximation (GGA) of Perdew and Wang[30] for exchange and correlation was applied, and electronic states were calculated for a $39 \times 39 \times 37$ Monkhorst−Pack mesh of points in reciprocal space.

Further self-consistent ab initio band structure calculations were also performed for LiNiN with the scalar relativistic tight-binding linear muffin-tin orbital (LMTO) method in the atomic spheres approximation, including the combined correction.[31−36] Within the LMTO formalism interatomic spaces are filled with interstitial spheres, and the optimal positions and radii of these additional "empty spheres" (ES) were determined by the procedure described in ref 37. Three non-symmetry-related ES with $0.62\ \text{Å} \leq r_{ES} \leq 1.41\ \text{Å}$ were introduced. The full LMTO basis set consisted of 4s, 4p, and 3d functions for Ni spheres, 2s, 2p, and 3d functions for Li and N spheres, and s, p, and d functions for ES. The eigenvalue problem was solved using the following minimal basis set obtained from the Löwdin downfolding technique: Ni 4s, 4p, 3d; N 2s, 2p; Li 2s and interstitial 1s LMTOs. The k space integration was performed using the tetrahedron method.[38] Charge self-consistency and the average properties were obtained from 2656 irreducible k points. A measure of the magnitude of the bonding was obtained by computing the crystal orbital Hamiltonian populations (COHP) which are the Hamiltonian population weighted density of states (DOS).[39] As recommended,[40] a reduced basis set in which all ES LMTOs have been downfolded was used for the COHP calculations.

Solid-State NMR. Wide-line ^{7}Li NMR spectra of powdered LiNiN were recorded at temperatures between 120 and 473 K and a Larmor frequency of 77.7 MHz. The home-built spectrometer used was based on a Resonance Instruments MARAN DRX pulse programmer and a 4.7 T Oxford Instruments superconducting magnet. Spectra were obtained using a solid-echo sequence with $\pi/2$ pulses of between 1.0 and 2.0 μs and an echo delay of 16.0 μs. Spin−lattice relaxation times were measured using the saturation recovery method, with a saturation sequence of $15\pi/2$ pulses separated by delays of the order of 1 ms. ^{7}Li and ^{6}Li MAS NMR spectra were recorded at Larmor frequencies of 116.6 and 44.2 MHz, respectively, using a Varian Infinityplus spectrometer and a 4 mm MAS probe with a MAS rate of approximately 15 kHz. Spectra were obtained using a rotor-synchronized spin−echo sequence with a $\pi/2$ pulse of 2.5 μs. Chemical shifts are referenced externally to aqueous LiCl.

Magnetic Susceptibility. Magnetic susceptibility measurements were performed on a Quantum Design MPMS XL 5T SQUID susceptometer in the temperature range 5−250 K, using powder samples loaded into gelatin capsules under an inert atmosphere (nitrogen-filled glovebox). All reported data were collected at an applied magnetic field of 1000 Oe and corrected for the diamagnetic contribution of the gelatin capsules.

Table 1. Crystallographic Parameters for LiNiN from Powder Neutron Diffraction

instrument, radiation	POLARIS TOF diffractometer, neutron		
sample	LiNiN		
temperature/K	100	200	280
crystal system	hexagonal		
space group	$P\bar{6}m2$		
Z	1		
M	79.648		
a-parameter/Å	3.73681(6)	3.73944(6)	3.74304(5)
c-parameter/Å	3.52527(7)	3.52511(7)	3.52542(6)
unit cell volume/Å^3	42.631(1)	42.689(1)	42.775(1)
calculated density, ρ_X / g cm^{-3}	3.102	3.098	3.092
observations, parameters	14609, 51	13439, 56	14609, 51
R_p	0.0173	0.0142	0.0164
R_{wp}	0.0113	0.0103	0.0098
X^2	2.191	1.906	1.655

Results

Structure Refinement. Initially, a structural model in space group $P\bar{6}m2$ was considered in which the Li stoichiometry is set to 1 and the Li atoms are constrained to occupy the 1b (0, 0, $^1/_2$) site, as determined previously from single-crystal X-ray diffraction.[3] Refinements employing this model, according to the procedure described in the Experimental Section, produced very good fits to the data ($R_{wp} \approx 1\%$) at each collection temperature, and no additional reflections were observed across the range of measured temperatures. Final crystallographic parameters are shown in Table 1, refined structural parameters in Table 2, and selected interatomic distances in Table 3. The structure from PND data is shown in Figure 1, and representative examples of profile fits are shown in Figure 2. Additional models in the same space group were considered and tested, but these produced higher residuals and goodness of fit values and/or physically unrealistic refined parameters. For example, relaxing the constraint on Li stoichiometry, resulted in 1b site occupancies greater than unity at each of the measured temperatures. Similarly, relaxing the stiochiometry constraint and allowing Li occupancy for both the 1b and the 1d ($^1/_3$, $^2/_3$, $^1/_2$) sites in the [LiN] plane to vary freely led to either negative site occupancies or negative thermal parameters. A model in which the Li stoichiometry was constrained to 1 and the fractional occupancies of both the above Li sites were allowed to vary, led to instabilities, lack of convergence and occupancies for the 1b and 1d sites greater and less than unity and zero, respectively.

Electronic Structure from ab Initio DFT Calculations. Figure 3 shows the band structure for LiNiN obtained using the FLAPW method as described in the Experimental Section, as well as the total DOS and the most important local partial DOS components. As expected from a structural model which

(23) Monkhorst, H. J.; Pack, J. D. *Phys. Rev. B: Condens. Matter Mater. Phys.* **1976**, *13*, 5188.
(24) Herzig, P. *Theor. Chim. Acta* **1985**, *67*, 323.
(25) Blaha, P.; Schwarz, K.; Herzig, P. *Phys. Rev. Lett.* **1985**, *54*, 1192.
(26) *MedeA* 2.0, Materials Design, Le Mans, France, and Taos (NM), USA, http://www.materialsdesign.com.
(27) Kresse, G.; Furthmüller, J. *Phys. Rev. B: Condens. Matter Mater. Phys.* **1996**, *54*, 11169.
(28) Kresse, G.; Furthmüller, J. *Computat. Mater. Sci.* **1996**, *6*, 15.
(29) Kresse, G.; Joubert, D. *Phys. Rev. B: Condens. Matter Mater. Phys.* **1999**, *59*, 1758.
(30) Wang, Y.; Perdew, J. P. *Phys. Rev. B: Condens. Matter Mater. Phys.* **1991**, *44*, 13298.
(31) Andersen, O. K. *Phys. Rev. B: Condens. Matter Mater. Phys.* **1975**, *12*, 3060.
(32) Andersen, O. K. *Europhys. News* **1981**, *12*, 4.
(33) Andersen, O. K. In *The Electronic Structure Of Complex Systems*; Phariseau, P., Temmerman, W. M., Eds.; Plenum Publishing Corporation, New York, 1984.
(34) Andersen, O. K.; Jepsen, O. *Phys. Rev. Lett.* **1984**, *53*, 2571.
(35) Andersen, O. K.; Jepsen, O.; Sob, M. In *Electronic Band Structure and Its Application*; Yussouf, M., Ed.; Springer-Verlag: Berlin, 1986.
(36) Skriver, H. L. *The LMTO Method*; Springer-Verlag: Berlin, 1984.
(37) Jepsen, O.; Andersen, O. K. *Z. Phys. B* **1995**, *97*, 35.
(38) Blöchl, P. E.; Jepsen, O.; Andersen, O. K. *Phys. Rev. B: Condens. Matter Mater. Phys.* **1994**, *49*, 16223.
(39) Dronskowski, R.; Blöchl, P. E. *J. Phys. Chem.* **1993**, *97*, 8617.
(40) Jepsen, O.; Andersen, O. K. Personal communication.

Table 2. Refined Atomic Parameters for LiNiN from Powder Neutron Diffraction

site	Li (0, 0, 1/2) (1*b*)			Ni (2/3, 1/3, 0) (1*e*)			N (2/3, 1/3, 1/2) (1*f*)		
T / K	100	200	280	100	200	280	100	200	280
$100 \times U_{11}$ / Å^2	0.4(2)	0.7(2)	0.5(2)	3.5(1)	2.33(7)	2.61(9)	2.6(1)	3.9(1)	3.8(1)
$100 \times U_{33}$ / Å^2	5.1(4)	5.3(5)	4.8(4)	1.25(8)	0.66(9)	0.8(2)	0.30(5)	0.8(1)	0.7(2)
$100 \times U_{12}$ / Å^2	0.18(8)	0.4(1)	0.27(9)	1.72(6)	1.17(4)	1.31(5)	1.28(5)	1.97(5)	1.88(6)

Table 3. Selected Interatomic Distances Obtained from Rietveld Refinements

T / K	Ni–N / Å	Li–N / Å	Ni–Ni / Å	Li–Ni / Å
100	1.7626(1) × 2	2.1575(1) × 3	3.7368(1) × 6	2.7859(1) × 6
200	1.7626(1) × 2	2.1590(1) × 3	3.7395(1) × 6	2.7871(1) × 6
280	1.7627(1) × 2	2.1610(1) × 3	3.7430(1) × 6	2.7888(1) × 6

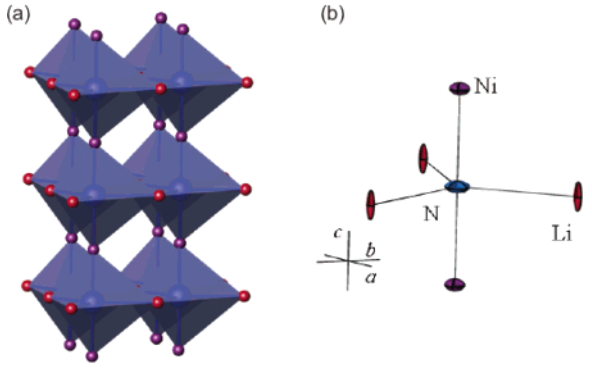

Figure 1. (a) Crystal structure of LiNiN at 280 K. Blue circles (within polyhedra) show the N atoms, red circles represent Li, and purple circles show Ni. (b) Coordination environment around N in LiNiN. Thermal ellipsoids are drawn at the 50% probability level.

might not suggest significant interchain interactions, the bands are rather flat, except in directions parallel to the *z*-axis of the Brillouin zone where they cross the Fermi level. This indicates that LiNiN exhibits a very anisotropic electronic conductivity. The band between about −14 and −12.8 eV is dominated by N 2s states with a Li 2s and 2p admixture. In the energy range from about −6.2 eV to the Fermi level there is a complex of bands which can be approximately divided into three regions distinguished by their bonding characteristics. Ni−N d_{z^2}−p_z σ-bonds are found in the lowest-energy region up to around −4.2 eV, with Ni−N (d_{xz}, d_{yz})−(p_x, p_y) π-interactions between −4.2 eV and the Fermi level, while additional Ni (d_{xy}, $d_{x^2-y^2}$) nonbonding states appear in the range between −1.5 and −0.6 eV. Figure 4 shows the valence electron densities for LiNiN in two planes. The density plot for the (110) plane visualizes the covalent bonds between Ni and N while weak interactions within the Ni layers stacked along the *c*-axis of the hexagonal structure are apparent from the plot in the (001) plane. The two types of bonding between the Ni and N atoms can be discerned in Figure 5, where the electron densities for two energy regions are given, i.e., from ∼−6.2 eV to −4.2 eV showing the Ni−N d_{z^2}−p_z σ-bonds and from −4.2 eV to the onset of the Ni (d_{xy},$d_{x^2-y^2}$) peak at roughly −2.2 eV showing the Ni−N (d_{xz},d_{yz})−(p_x,p_y) π-bonds.

Crystal orbital Hamiltonian populations (COHP) computed for different contacts in LiNiN obtained using the TB-LMTO-ASA program are shown in Figure 6. Integrated COHP (ICOHP) values of −0.41 and −0.03 Ry/cell were obtained for the shortest Ni−N and Li−N contacts, respectively. It should be noted that Ni−Ni interchain ICOHP absolute values lower than 0.01 Ry/cell were calculated. These results corroborate the

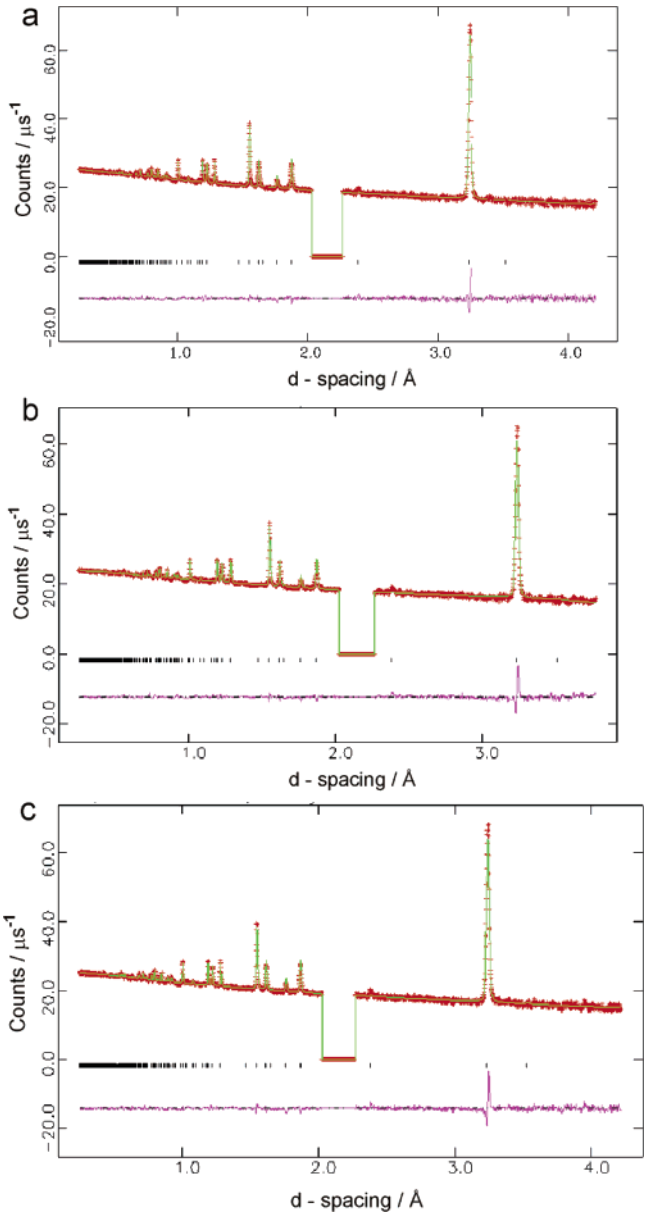

Figure 2. Observed, calculated, and difference profile plots for the Rietveld refinement of PND data for LiNiN at (a) 280, (b) 200, and (c) 100 K. Crosses show the observed data points, solid lines represent the calculated diffraction patterns, and tick marks represent the calculated positions of the reflections. Bragg reflections from the vanadium in the cryostat vacuum windows and the sample can are excluded from the refinements. The data shown are from detectors at $2\theta = \langle 90° \rangle$.

primarily 1D nature of the electronic structure of LiNiN, suggested by the FLAPW calculations. Assuming a rigid band model, the Ni−N COHP curve suggests that lengthening of the Ni−N contact within the chain is foreseen upon reduction of the chains. This comes from the π Ni−N antibonding character of the band that crosses the Fermi level.

The Fermi surface of LiNiN is shown in Figure 7. As already indicated by the band structure, three bands contribute to the

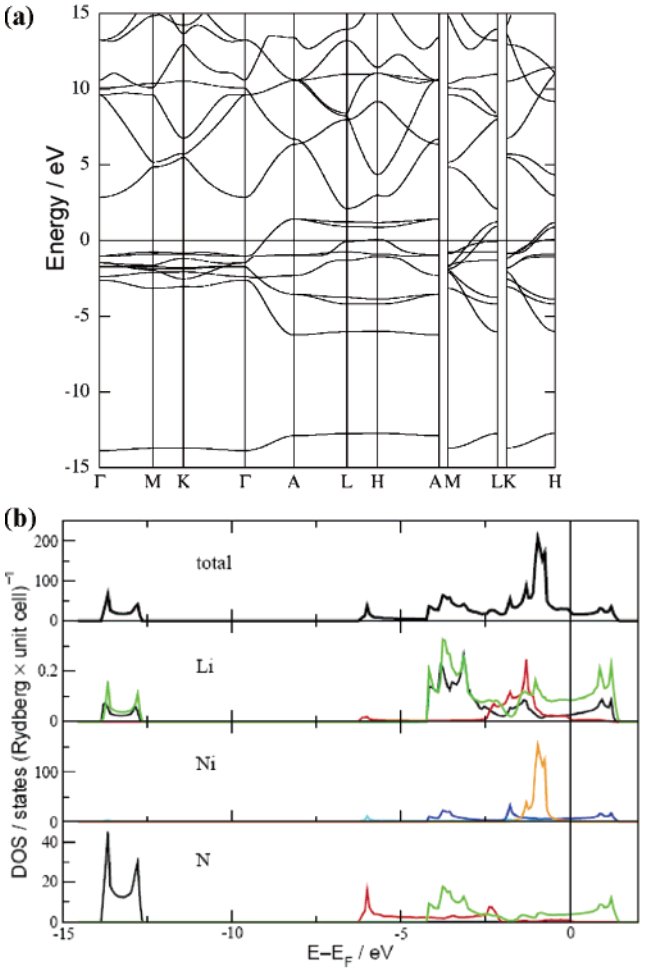

Figure 3. Band structure (a) and DOS per Rydberg per formula unit (b) for LiNiN. In (b) the local partial DOS components are: s black, p_z red, p_x, p_y green, d_{z^2} cyan, d_{xz}, d_{yz} blue, d_{xy}, $d_{x^2-y^2}$ orange. Note the different scales of partial and total DOS components.

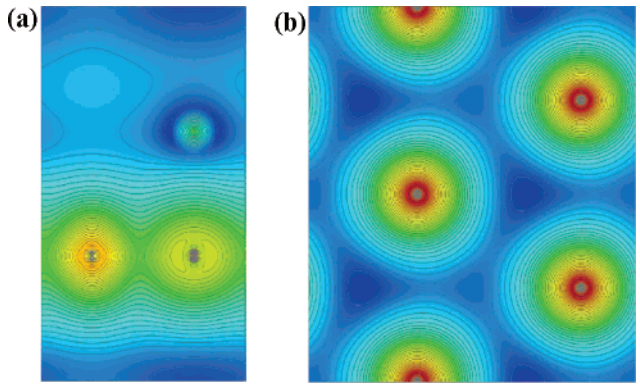

Figure 4. Valence electron densities for LiNiN: (a) (110) plane through Li (upper right), Ni (lower left), N (lower right); (b) (001) plane through Ni atoms. A logarithmic grid of contour lines has been used ($x_i = x_0 2^{i/3}$, $x_0 = 0.0002$ e Å^{-3}).

Fermi surface, and hence to electrical conductivity. Band 8 contributes the narrow pocket close to the H point, while most of the surface is determined by bands 9 and 10. In the band structure of Figure 3a these bands are cut by the Fermi energy in directions parallel to the *c*-axis, specifically Γ−A, M−L, and K−H. They are only degenerate along the Γ−A axis, and away from this symmetry line they form parallel sheets perpendicular

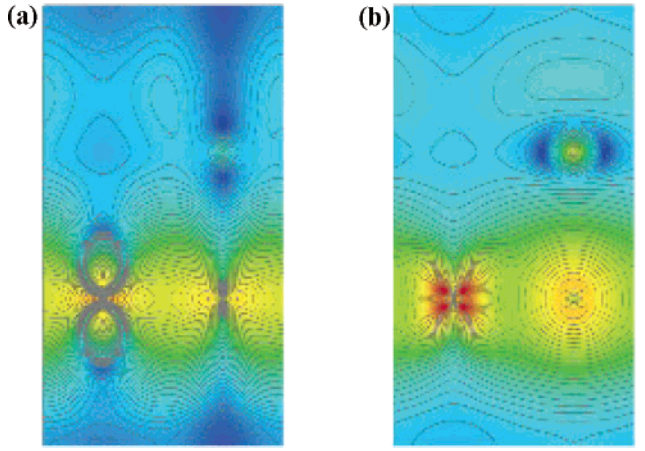

Figure 5. Electron densities in the (110) plane for LiNiN (Li: upper right, Ni: lower left, N: lower right) in energy ranges (a) −6.2 to −4.2 eV and (b) −4.2 to −2.2 eV, corresponding to Ni−N σ- and π-bonds, respectively. A logarithmic grid of contour lines has been used ($x_i = x_0 2^{i/3}$, $x_0 = 0.0002$ e Å^{-3}).

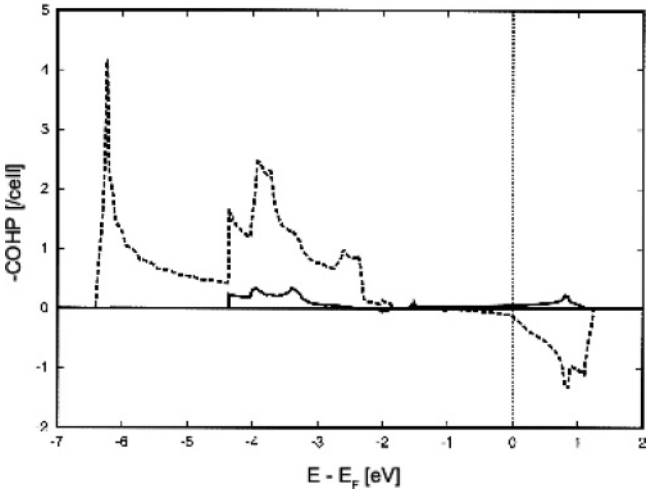

Figure 6. Li−N (solid) and Ni−N (dotted) COHP curves calculated for LiNiN.

to the *c*-axis. The exceptional topology of the Fermi surface of LiNiN suggests anisotropic electrical conductivity.

Further information on electronic structure and bonding can be obtained from the electric-field gradient (EFG). For its calculation a proper description of the higher-lying core states ("semicore") is essential. Calculated EFG values can be split into the contribution of the sphere around the respective atoms ("sphere contribution") and the remainder of the crystal lattice. The sphere contribution can be further separated into ll′-like contributions, of which only sd, pp, and dd are important, if f electrons do not play a role.

For LiNiN the EFG tensors for all three atoms have been calculated. Since all the atoms occupy sites with $\bar{6}m2$ (D_{3h}) symmetry, there is no asymmetry parameter and the EFG tensor is fully defined by just one number (V_{zz}). The total values and the sphere and most important ll′-like contributions (including the semicore pp contribution for Ni) are given in Table 4. For LiNiN the principal axes corresponding to the V_{zz} components are always oriented in direction of the *c*-axis, and since negative EFG components indicate strong interactions with neighboring atoms, the results can be interpreted as follows. The strongest Li interactions are within the *ab* plane and are directed toward

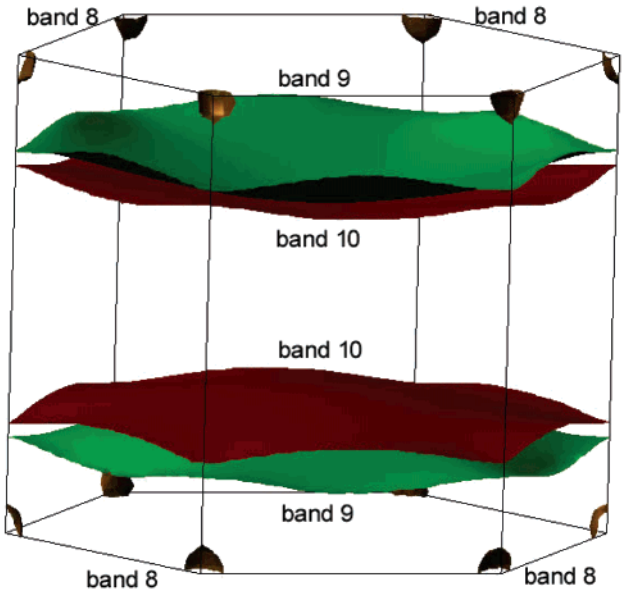

Figure 7. Fermi surface of LiNiN showing band 8 in brown, band 9 in green, and band 10 in red/maroon.

Table 4. Total V_{zz} Values, Sphere Contributions, and Most Important ll' Contributions in Units of 10^{20} V m^{-2}

	Li	Ni	N
total	1.5	23.0	−63.8
sphere	0.7	19.7	−79.6
pp	0.6	−330.4	−70.0
pp (semicore)	0.0	29.1	−0.1
dd	0.0	325.0	−0.4

the N atoms while for N they are oriented in the *c* direction toward the Ni atoms. The situation for Ni is more complicated. The large negative pp contribution originates from Ni−N interactions in the *c* direction and the similarly large positive dd contribution from Ni−Ni interactions in the (001) plane. The semicore pp contribution is not directly influenced by the atomic neighbors, but only indirectly by the polarizing effect of the valence electrons on the semicore states and usually carries the opposite sign of the valence-electron contribution. The fact that the pp component for Ni is about as large as the dd component (although the p contribution to the DOS is much smaller than the d contribution) is due to the slower increase of the 3d wave function near the nucleus compared to the 4p wave function.

Solid-State NMR. Variable-temperature wide-line ^{7}Li spectra of LiNiN were discussed briefly in our previous communication[4] and are shown in Figure 8. Since the quadrupole moment of ^{7}Li is relatively small, the single Li site expected from the $P\bar{6}m2$ space group should result in a narrow central line, flanked by a single pair of first-order powder-broadened satellite lines. The value of the EFG (eq) of 1.5×10^{20} V m^{-2} obtained from the density functional calculations described above, together with a ^{7}Li quadrupole moment (Q) of -40.1×10^{-31} m^2,[41] suggests that the quadrupolar coupling constant $C_Q = e^2qQ/h$ should be 145 kHz. An uncertainty in this calculated value of no more than 15% is expected by comparison with the success of similar calculations for the parent Li_3N.[25] However, at low temperatures the spectrum for LiNiN is dipolar broadened to the extent that the quadrupolar satellites are lost in the baseline and the coupling

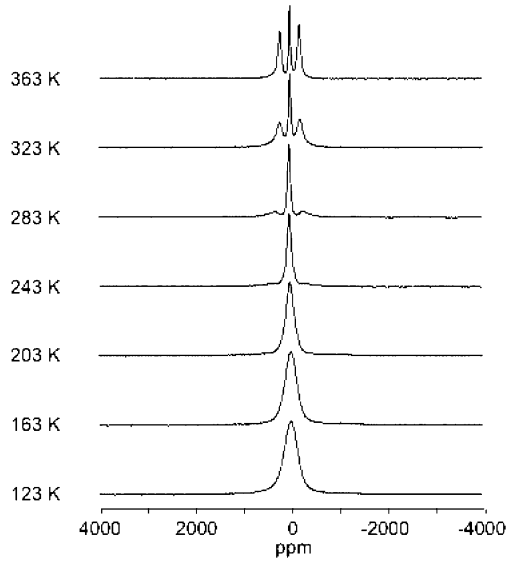

Figure 8. Variable-temperature wide-line ^{7}Li spectra of LiNiN, recorded as described in the text.

constant cannot be measured directly from the spectrum. Between 160 and 300 K motional narrowing of the central transition is observed, arising from diffusion of Li^+ in the [LiN] planes. As described previously,[4] the extent of motional narrowing suggests a correlation time for Li^+ hopping of 3.5 μs at room temperature. Although the low-temperature broadening of the central transition is dipolar in origin, the possibility exists that the satellites are additionally broadened by a distribution of quadrupolar couplings resulting from variations in EFG. Above 280 K a single pair of satellites with a splitting of approximately 40 kHz starts to emerge without any further significant narrowing of the central transition. These satellites do not show the expected Pake line shape for a powder sample, whereas the splitting is about one-half of that expected from the calculated EFG, even including the 15% uncertainty noted above. This could suggest that these satellites result from a partial averaging of the low-temperature EFG distribution due to the diffusion of the Li^+ ions in the [LiN] plane, since the measured room-temperature hopping time is short enough to achieve this. We note that the spectra vary with temperature in a similar fashion to the "universal" behavior observed previously[42] for LISICON and phosphate Li superionic conductors, although in those cases Pake-type lineshapes with reduced quadrupolar coupling constants indicative of a specific anisotropic motion were observed at high temperatures.

^{7}Li MAS spectra are shown in Figure 9 for temperatures of 298 K (9a) and 153 K (9b), as well as a ^{6}Li MAS spectrum (9c) recorded at room temperature. All spectra were recorded at a MAS rate of 15 kHz and are referenced externally to aqueous LiCl. A spectral range of 2000 ppm was chosen in each case, such that the corresponding frequency ranges are 233 kHz for (9a) and (9b) and 88 kHz for (9c). In paramagnetic solids the MAS centerband frequency and the sideband intensities can depend on the hyperfine interaction between nuclear spins and electronic moments.[43] The isotropic Fermi contact interaction with s-state unpaired electrons results in a shift in the MAS centerband frequency which depends on the hyperfine coupling constant and the magnetic susceptibility of the

(41) Pyykkö, P. *Mol. Phys.* **2001**, *99*, 1617.

(42) Bertermann, R.; Müller-Warmuth, W. *Z. Naturforsch.* **1998**, *53a*, 863.

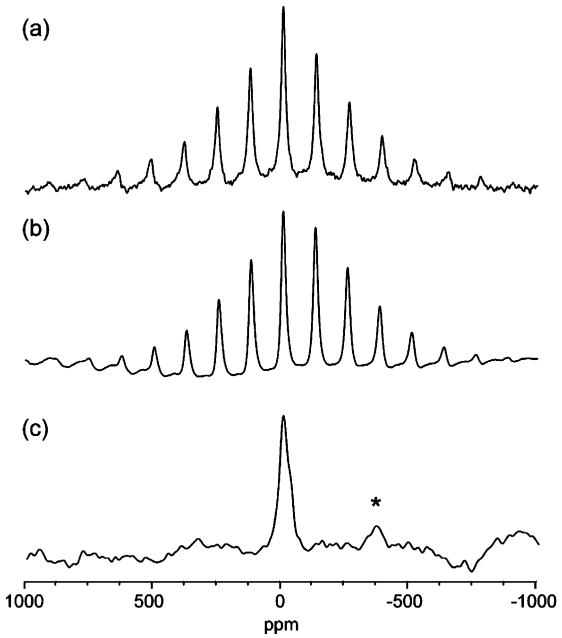

Figure 9. ^{7}Li MAS NMR spectra recorded as described in the text at (a) 298 K and (b) 153 K, along with the corresponding room temperature ^{6}Li MAS NMR spectrum. Note that a constant ppm range has been chosen, and that the asterisk indicates a single MAS sideband in (c).

electrons. Anisotropic dipolar interactions with unpaired electrons in non s-states contribute to the MAS sidebands and, in cases where the electronic **g** tensor is also anisotropic, result in an additional isotropic "pseudocontact" shift.[44] The temperature variation of the dominant Fermi contact interaction results directly from that of the susceptibility, such that Curie−Weiss paramagnetism leads to a temperature-dependent shift. In metallic systems Pauli paramagnetism is associated with a (largely) temperature-independent susceptibility, resulting in a temperature-independent Fermi contact shift, often called the Knight shift. A comparison of a and b of Figure 9 shows that the resonance frequency of the center band is essentially independent of temperature, shifting from −2 ppm at 153 K to −4 ppm at 298 K, relative to aqueous LiCl. The centerband frequency for ^{6}Li is identical, as expected. This small Knight shift is consistent with the band structure calculations described above which indicate that the Li s-state partial DOS in the region of the Fermi level is small, and hence, it provides further evidence for the metallic nature of LiNiN. Note that our previous report of a temperature-independent 30 ppm shift was less accurate due to the slower MAS rate used in those experiments. For ^{7}Li an extensive spinning sideband manifold is observed at both temperatures, whereas for ^{6}Li at room temperature the spinning sidebands are almost completely absent. This striking difference suggests that the sidebands in (a) and (b) are largely quadrupolar in origin, since the quadrupole moment of ^{6}Li is some 50 times smaller than that for ^{7}Li.[41] Dipolar interactions, including those associated with paramagnetism mentioned above, would not scale so dramatically, since the magnetogyric ratio of ^{6}Li is only 2.6 times smaller than that for ^{7}Li.

Magnetic Susceptibility Measurements. As shown in Figure 10 the magnetic susceptibility of LiNiN shows only a small temperature dependence, suggesting the Pauli paramagnetism

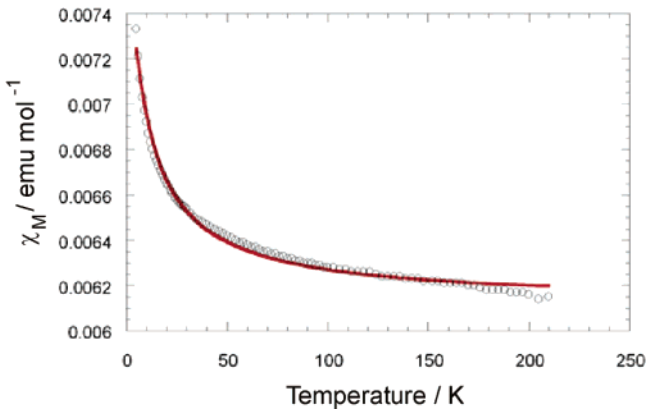

Figure 10. Molar susceptibility as a function of temperature for LiNiN. The solid line shows the fit to eq 2.

expected for a metallic compound. A small Curie−Weiss contribution is observed at temperatures below 50 K, and so the magnetic susceptibility can therefore be described by a modified Curie−Weiss (C−W) law

$$\chi_{M} = \chi_0 + \frac{C_M}{T - \theta} \qquad (2)$$

where χ_M is the molar susceptibility, χ_0 is a temperature-independent term, C_M is the molar Curie constant, and θ is the Weiss constant. Fitting of the magnetic susceptibility data to eq 2 yielded the following best-fit parameters: $\chi_0 = 6.126(6) \times 10^{-3}$ emu mol^{-1}, $C_M = 0.0158(5)$ emu mol^{-1} K, and $\theta = -9.1(5)$ K. The value of the effective magnetic moment for Ni atom, $\mu_{eff} = 0.36\ \mu_B$, suggests the formation of a delocalized (itinerant) spin system typical for metallic compounds. No evidence of a magnetic ordering transition was observed in the data, in agreement with PND data over the temperature range studied. The relatively small C−W component might arise from local defects in the structure where, for example, Li atoms occupy the interplanar Li(1) site and disrupt the continuity of the $^{1}_{\infty}[NiN_{2/2}]^{-}$chains. Similar small, localized Ni moments are observed in CaNiN where no substitutional discontinuities in the $^{1}_{\infty}[NiN_{2/2}]^{2-}$ chains are expected, but where point defects have been suggested.[7,45] CaNiN samples in both previous experimental studies also contained Ni impurities. No impurity phases were observed in LiNiN samples within the detection limits of PND.

The Weiss constant shows a relatively small deviation from zero in contrast to results obtained for the disordered compounds $Li_{3-x-y}Ni_xN$, where much larger negative values were reported at high Ni substitution levels (e.g., $x = 0.85$; $\theta = -85$ K).[5b] These negative values were attributed to anti-ferromagnetic exchange interactions between the transition metal ions.[5b] By contrast, the value of the Weiss constant for LiNiN, coupled with lack of evidence for a magnetic transition in both susceptibility and PND data, implies the absence of strong anti-ferromagnetic interactions and any long-range magnetic ordering in this compound.

Discussion

The structure of LiNiN derived from PND data is essentially in very close agreement with the model from single-crystal

(43) Gee, B.; Horne, C. R.; Cairns, E. J.; Reimer, J. A. *J. Phys. Chem. B* **1998**, *102*, 10142.
(44) Nayeem, A.; Yesinowski, J. P. *J. Chem. Phys.* **1988**, *89*, 460.
(45) Shamoto, S.; Kato, T.; Ohoyama, K.; Ohashi, M.; Yamaguchi, Y.; Kajitani, T. *J. Phys. Chem Solids* **1999**, *60*, 1157.

X-ray diffraction and is described fully in ref 3. The models derived from both diffraction techniques describe layered structures derived from Li_3N that differ primarily from the parent compound first in the composition of the metal layer (Ni vs Li) and second in the location and distribution of lithium in the [Li−N] plane (50% of the lithium content found in the $[Li_2N]$ planes of Li_3N is present in the [LiN] planes in LiNiN, and alkali metal vacancies are ordered on three-coordinate 1d positions within the plane—resulting in a lowering of symmetry from *P*6/*mmm* to $P\bar{6}m2$). The complete substitution of Ni for Li at the interplanar Li(1) site, as verified by the PND model, creates continuous, infinite, straight $^1_\infty[NiN_{2/2}]^-$ chains along the *c*-direction which begin to form at lower substitution levels in the disordered relatives $Li_{3-x-y}Ni_xN$.[8,46,47] This structure is retained over the temperature range investigated. Although there is an overall unit cell volume increase from 100 to 280 K as expected, it is interesting to note that anisotropic negative thermal expansion appears to be exhibited in the [001] direction from 100 to 200 K (with a commensurate apparent decrease in the Ni−N bond length with increasing temperature). Statistically, the *c*-parameter is constant from 100 to 200 K (1.6σ) and increases slightly from 200 to 280 K (3.4σ). This, to some extent, mirrors the situation in Li_3N where the *c*-parameter remains almost invariant between 10 and 888 K.[48] Additional data for LiNiN would need to be collected at lower and intermediate temperatures to clarify the extent of this effect.

The Li−N and Ni−N bond distances at 280 K (listed in Table 3) are similar to those reported at 297 K in the original X-ray study.[3] Two-coordinate Ni−N units form with bond lengths closely matching those found in other linear $^1_\infty[NiN_{2/2}]^{n-}$ chains, e.g., 1.790 Å in CaNiN[7] and 1.773 Å and 1.778 Å in $Li_3Sr_3Ni_4N_4$.[8] The reduced interplanar distance in LiNiN over Li_3N confirms previous observations of contraction as Ni progressively replaces Li in the Li(1) position. The premise that the Ni−N bond length is reduced vs Li−N as a result of increased covalency is corroborated by our band structure and electron density calculations which show significant N 2p−Ni 3d π-interactions. The degree of Ni−N covalency has implications for the classification of LiNiN as a formal Ni(II) compound despite the empirical evidence from bond valence (BV) calculations,[49] taken for distances here just as in the original X-ray study. Valence sums for the PND 280 K model yield values of Li: 0.7, Ni: 1.9, N: −2.6. Of note is the low positive valence for Li and the higher than expected sum for N. Similar values are calculated for Li_3N and ostensibly suggest incomplete charge transfer. Although since BV values are empirical in origin and calculated oxidation states can differ significantly from those derived theoretically, there is some agreement between BV and FLAPW descriptions of bonding. The latter DFT methods illustrate that there is evidence for Li−N bonding in the energy region of the N s band (∼13−14 eV below E_F) and also ∼2−4 eV below E_F. These interactions are also noticeable in the DOS (Figure 3b). Arguments from EELS measurements have also been proposed for $Li_{3-x-y}Co_xN$ materials that N is oxidized with increasing *y*[13] and previous XAS results for $Li_{3-x-y}M_xN$ (M= Ni, Cu) for varying *x* (and likely very small values of *y*) indicate only small (but significant) shifts in the M K-edge from the elemental metals to $Li_{3-x-y}M_xN$.[5b] Further, the PND model describes a structure in which nickel atoms from neighboring chains are separated by 3.75 Å. Given that CaNiN and the title compound share some structural aspects, it is interesting to compare their electronic structure. A strong 1D character to the electronic properties of CaNiN has been demonstrated by Springborg et al.[12] However, interaction of the calcium atoms with the Ni−N chains in CaNiN is not solely ionic but also contains a significant covalent component. This confers some "pseudo-three-dimensional" properties to the electronic structure of CaNiN. Such a contribution from the lithium atoms is not so straightforward in LiNiN since the alkali metal contribution to the occupied bands is very small. The increased Ni···Ni distances in LiNiN compared to those in CaNiN (3.5809 Å between parallel $^1_\infty[NiN_{2/2}]^{2-}$ chains, 3.5048 Å between perpendicular $^1_\infty[NiN_{2/2}]^{2-}$ chains) might suggest the absence of significant electronic interactions between the individual chains,[7] yet DFT calculations illustrate that, just as in the calcium compound, these long-distance interactions play a small but significant role in the electronic structural configuration of the nitridonickelate and may be pivotal in the determination of electronic properties. In this context, it is also notable that, just as no evidence of magnetic ordering or CDW instabilities was observed here in LiNiN, neither were any long-range effects observed in a recent study of CaNiN.[45]

The PND model for LiNiN also permits some further comparison of the structural features of the ordered compound with the disordered phases $Li_{3-x-y}Ni_xN$ ($0 \le x \le 0.8$) and associated implications for the transport properties in these materials. The increased occupancy of the interplanar site by Ni in LiNiN over the $Li_{3-x-y}Ni_xN$ compounds leads to the formation of continuous $^1_\infty[NiN_{2/2}]^-$ chains of increased covalent character cf. $^1_\infty[(Li,Ni)N_{2/2}]^{n-}$ and a reduction in *c*-parameter in LiNiN compared to $Li_{1.36}Ni_{0.79}N$, for example.[46] Likewise, the $^1_\infty[NiN_{2/2}]^-$ chains in LiNiN lead to metallic behavior, which is first evidenced in $x \approx 0.8$ materials, which is the composition proposed to be near the semiconducting-metal transition.[5b] Li^+ vacancies are disordered within the $[Li_{2-y}N]$ planes in the $Li_{3-x-y}M_xN$ (M = Co−Cu) compounds, and from the large anisotropic thermal parameters found in these materials, Li^+ would appear to be mobile.[46,47,50] Additionally, the disordered phase $Li_{3-x-y}Cu_xN$ shows diffusion coefficients and relaxation times which are comparable to those of the parent compound Li_3N.[4,6] By contrast to the nitridocuprate and Li_3N itself, the ordered compound LiNiN shows less pronounced anisotropy in the thermal parameters and a reduced diffusion coefficient at ambient temperature from NMR results, despite exhibiting a lower activation energy for Li^+ intraplanar diffusion.[4] The PND data for LiNiN provide a model of the long-range structure that implies that Li^+ populates only the 1b site and that the vacant 1d site is not occupied. However, the apparent broadening of the satellites in the low-temperature NMR spectra suggest local structural disorder in addition to the ionic motion in [LiN] planes indicated by the line narrowing at higher temperatures. From the combination of models, therefore, one might envisage (a) diffusion of Li^+ ions between 1b sites, although the Li···Li distance is now significantly

(46) Gregory, D. H.; O'Meara, P. M.; Gordon, A. G.; Hodges, J. P.; Short, S.; Jorgensen, J. D. *Chem. Mater.* **2002**, *14*, 2063.
(47) Stoeva, Z.; Smith, R. I.; Gregory, D. H. *Chem. Mater.* **2006**, *18*, 313.
(48) Zucker, U. H.; Schulz, H. *Acta Crystallogr.* **1982**, A*38*, 568.
(49) Brese, N. E.; O'Keeffe, M. *Acta Crystallogr.* **1991**, B*47*, 192.
(50) Gordon, A. G.; Smith, R. I; Wilson, C.; Stoeva, Z.; Gregory, D. H. *Chem. Commun.* **2004**, 2812.

increased compared to that in Li_3N (3.74 Å vs 2.11 Å) and no Li^+ vacancies are indicated on the 1b site by PND or (b) the hopping of Li^+ ions from one occupied 1b site to the next via the vacant 1d site (now effectively an interstitial). We are currently investigating the entire $Li_{3-x-y}Ni_xN$ series ($0 \leq x \leq 0.8$; $x = 1$, $y = 1$) to develop a more cohesive understanding of the evolution of Li^+ ion-transport behavior and structure with x. Effectively, one might control the degree of ionic and electronic conductivity through synthesis conditions (and thus in turn x and y)[47] and perhaps also by judicious tuning of relative multimetallic substituent levels (d-electron concentrations) on the interplanar site in both ordered and disordered nitridometalates. Such studies with quaternary and higher compounds are now also being pursued in our laboratory.

Conclusions

Our structural investigation of the ternary nitride LiNiN using PND confirms that this compound has an ordered structure which is derived from the well-established structure of α-Li_3N. Ordering results from the preferred occupation of the 1b (0, 0, $^1/_2$) site by the lithium atoms in LiNiN in contrast to α-Li_3N where lithium atoms 98% occupy the ($^1/_3$, $^2/_3$, 0) site (in space group $P6/mmm$). The nickel atoms only occupy the interlayer 1e ($^2/_3$, $^1/_3$, 0) site in LiNiN resulting in the formation of infinite straight $^1_\infty[NiN_{2/2}]^-$ chains with no evidence of electronically driven distortions. The first-principle DFT calculations confirm the premise that the nickel−nitrogen chains are responsible for the appearance of metallic properties as manifested by the predominantly Pauli-type paramagnetic behavior observed experimentally. The Fermi level is primarily dominated by contributions from nickel d levels and nitrogen p orbitals, and lithium states make no significant contribution to the DOS at the Fermi level. The absence of a significant shift in the ^7Li MAS NMR resonance line is in accord with the metallic nature of the material and again confirms that lithium makes little or no contribution to the DOS at E_F. This evidence for metallic properties, in addition to the observation of fast Li^+ ion diffusion, suggests that LiNiN is a promising candidate for application as an anode material in lithium ion batteries.

Acknowledgment. This work was supported by EPSRC (UK) Grant GR/R87345. The CCLRC (UK) is acknowledged for the award of beam time at ISIS and the authors thank Dr R.I. Smith (ISIS, RAL, UK) for his help in collecting neutron data on POLARIS. Financial support from the Austrian Science Foundation (project no. P15801−N02) is acknowledged. Some of the calculations were performed on the Schrödinger II Linux cluster of the Vienna University Computer Centre.

Supporting Information Available: Simulation of ^7Li MAS-NMR spectrum for LiNiN. This material is available free of charge via the Internet at http://pubs.acs.org.

JA063208E